NUMERICAL SOLUTION OF THE SCHRÖDINGER EQUATION

Amir Assadi and Jie Yeong Tan
11313050 and your 11010638

Department of Physics and Astronomy
The University of Manchester

Second Year Computing Project

April 2025

Abstract

This project numerically solves the one-dimensional and two-dimensional Schrödinger equation for infinite wells and perturbed systems using finite difference and Crank-Nicolson methods. For unperturbed wells, eigenstate matched with analytical solutions within an accuracy of 0.2% for the first four energy levels, with perfect wavefunction overlap. Introducing a half-quantum simple harmonic oscillator (HQSHO) perturbation yielded odd-parity eigenstates but increased energy errors to between 0.2% and 0.8%. In two-dimensional systems, degeneracy and 3.5–3.6% energy errors were observed. Time evolution revealed wave packet interference and reflections, with HQSHO perturbations altering dynamics. The methods reliably model quantum systems, though accuracy degrades for complex potentials.

1. Introduction

In 1926, Austrian physicist Erwin Schrödinger formulated his famous equation which revolutionized modern physics [1]. Later-dubbed the Schrödinger equation, solving it provides quantized energy levels and the wavefunction of a quantum system, which are important for understanding atomic and subatomic phenomena.

The investigation of quantum systems under different potential landscapes, including barriers and wells, holds particular significance for modern physics and technology. Quantum mechanical phenomena such as tunnelling, where particles traverse classically forbidden regions, find practical applications in devices ranging from scanning tunnelling microscopes to flash memory. Similarly, the study of quantum wells formed by confining potentials underpins the operation of semiconductor lasers and other optoelectronic components. Furthermore, perturbed potential systems serve as models for understanding molecular interactions and engineered nanoscale structures.

This project focuses on numerical solutions to both the time-independent and time-dependent forms of the Schrödinger equation. Our primary objectives involve employing the finite difference method to solve for eigenstates and eigenenergies in various potential configurations, including infinite wells and perturbed systems, while applying perturbation theory to analyse resulting energy level modifications. For time-dependent phenomena, we implement the Crank-Nicolson method [2] to simulate wave packet dynamics and investigate quantum tunnelling effects. Additionally, we extend these computational approaches from one-dimensional to two-dimensional systems, enabling examination of degeneracy effects and interference patterns that emerge in higher-dimensional quantum systems. Through this work, we demonstrate the powerful synergy between fundamental quantum theory and modern computational techniques in advancing our understanding of quantum phenomena.

2. Theory

This section outlines the equations and methods used in our numerical solutions. The Schrödinger equation defines the eigenvalue problem and time evolution, while the finite difference method [3] discretizes it for computational solving. For dynamics, the Crank-Nicolson scheme ensures stable propagation. Perturbation theory predicts energy shifts, and 2D extensions generalize the approach [4]. Finally, transmission coefficients benchmark tunnelling results.

2.1. Schrödinger Equation in 1D

The time-independent Schrödinger equation (TISE) in one dimension is given by

$$-\frac{\hbar^2}{2m}\frac{d^2\psi(x)}{dx^2} + V(x)\psi(x) = E\psi(x) \, , \tag{1}$$

where $\psi(x)$ is the wavefunction, $V(x)$ is the potential, and E is the energy eigenvalue, $\hbar$ is the reduced Planck constant, and m is the particle mass. The time-dependent Schrödinger equation (TDSE) describes dynamical evolution:

$$i\hbar \frac{d\psi(x,t)}{dt} = \left[-\frac{\hbar^2}{2m}\frac{d^2}{dx^2} + V(x)\right]\psi(x,t). \tag{2}$$

Boundary conditions for confined systems (e.g., infinite wells) require $\psi(x) \to 0$ at boundaries, and the wavefunction must be normalized such that

$$\int |\psi(x)|^2 \, dx = 1. \tag{3}$$

2.2. Finite Difference Method

The finite difference method approximates derivatives by discretizing space into a grid with spacing Δx. The second derivative becomes:

$$\frac{d^2\psi}{dx^2} \approx \frac{\psi_{i+1} - 2\psi_i + \psi_{i-1}}{(\Delta x)^2}, \tag{4}$$

yielding a matrix eigenvalue problem

$$H\psi = E\psi, \tag{5}$$

where H is a tridiagonal Hamiltonian matrix. Accuracy depends on Δx (smaller Δx reduces error but increases computational cost), and stability requires $\Delta x \ll$ the characteristic length scale of $V(x)$.

2.3. Crank-Nicolson Method

For the TDSE, the Crank-Nicolson scheme provides a unitary and stable time propagation:

$$\left(I + \frac{i\Delta t}{2\hbar}H\right)\psi^{n+1} = \left(I - \frac{i\Delta t}{2\hbar}H\right)\psi^n, \tag{6}$$

where I is the identity matrix and Δt is the timestep. This implicit method is unconditionally stable for Hermitian Hamiltonians and preserves norm conservation.

2.4. Perturbation Theory

For small perturbations H' to a solvable Hamiltonian H'_0, the first-order energy correction is

$$E_n^{(1)} = <\psi_n^{(0)}|H'|\psi_n^{(0)}>, \tag{7}$$

where $\psi_n^{(0)}$ are unperturbed eigenstates.

Second-order corrections account for mixing with other states:

$$E_n^{(2)} = \sum_{m \neq n} \frac{\left|<\psi_m^{(0)}|H'|\psi_n^{(0)}>\right|^2}{E_n^{(0)} - E_m^{(0)}}. \tag{8}$$

In our system, the potential is perturbed by a harmonic term

$$V(x) = V_0(x) + \frac{1}{2}m\lambda\omega^2 x^2, \tag{9}$$

where λ is a dimensionless coefficient of perturbation and $V_0(x)$ is the unperturbed potential.

For the case where $V_0(x)$ is the infinite square well of width L, the corrected energy levels due to the perturbation $H' = \frac{1}{2}m\lambda\omega^2 x^2$ are

3

$$E_n = \frac{n^2\pi^2\hbar^2}{2mL^2} + \lambda\frac{m\omega^2L^2}{8}\left(1 - \frac{6}{n^2\pi^2}\right), \tag{10}$$

2.5. Extension to 2D

In 2D, the Laplacian ∇^2 is discretized using a 5-point stencil:

$$\nabla^2\psi \approx \frac{\psi_{i+1j}+\psi_{i-1j}+\psi_{ij+1}+\psi_{ij-1}+4\psi_{ij}}{(\Delta x)^2}. \tag{11}$$

The Hamiltonian becomes block-tridiagonal, and boundary conditions must be enforced on all edges (e.g., $\psi = 0$ for infinite wells). The Crank-Nicolson scheme extends naturally to 2D but requires solving larger sparse linear systems.

2.6. Reflection and Transmission coefficients

When a quantum particle with energy E encounters a potential barrier of height $V_0 > E$ and width a, its transmission probability T is governed by the expression

$$T = \left[\frac{16k^2\beta^2}{(\beta^2+k^2)^2}\right]e^{-2\beta a}, \tag{12}$$

where $k = \frac{\sqrt{2mE}}{\hbar}$ represents the incident wave vector and $\beta = \frac{\sqrt{2m(V_0-E)}}{\hbar}$ characterizes the wavefunction's decay within the barrier. The reflection coefficient follows as

$$R = 1 - T, \tag{13}$$

ensuring probability conservation. This analytical solution, derived for ideal rectangular barriers, provides a benchmark for our numerical simulations.

3. Implementation

3.1. Computational Setup

The project was developed in Python 3.9, making use of SciPy's sparse linear algebra routines and NumPy for efficient array operations. Spatial discretization employed uniform grids with resolutions carefully selected to resolve quantum mechanical features while maintaining computational efficiency. For instance, one-dimensional systems utilized grid spacings of Δx = 0.04-0.40 Å, while two-dimensional implementations employed square grids with Δx = Δy = 0.2-1.0 Å.

Temporal evolution in time-dependent simulations adopted adaptive timesteps (Δt = 10^{-4} to 0.1 fs) that satisfied the stability criteria of the Crank-Nicolson scheme. Physical constants were implemented using SciPy. Constants ($\hbar$ = 1.05×10^{-34} J·s, m_e = 9.11×10^{-31} kg), with an optional dimensionless mode ($\hbar = m = 1$) for simplified test cases.

The potential energy landscape implementation supported both analytical forms (harmonic oscillator, Coulomb potential) and piecewise-defined barriers with

configurable parameters, including barrier widths (0.05-1.5 nm), potential heights ($\pm 10^4$ eV), and multi-slit configurations (2-5 slits). Boundary conditions were enforced through infinite potential walls ($V = 10^{10}$ eV) at domain edges, with Neumann conditions implemented via ghost points where applicable. This comprehensive setup enabled investigations ranging from single-particle quantum wells to complex 2D tunnelling systems.

3.2. Code Structure

The code centred around three core components working in tandem. The eigenstate solver formed the foundation, constructing Hamiltonian matrices through finite differences for 1D systems and Kronecker products for 2D cases. For systems under 1000 grid points, it used precise direct diagonalization, while larger problems leveraged memory-efficient iterative methods. Built-in wavefunction normalization and phase correction ensured physically meaningful results every time.

Next is the time evolution engine, which implemented the Crank-Nicolson scheme to preserve quantum probabilities perfectly. By precomputing the Lower-Upper decomposition upfront, we achieved fast time-stepping without sacrificing accuracy. This versatile engine handled both real-time quantum dynamics and imaginary-time ground state searches, automatically tuning its time steps for optimal performance.

The perturbation module quantified how quantum systems respond to external influences. It accurately calculated energy shifts from simple perturbations like λx^2 potentials to more complex interactions, including those involving degenerate states. The module's numerical integration approach provided reliable results across all these scenarios.

We validated the implementation through multiple approaches. Convergence testing refined grids and time steps until results stabilized, while comparisons against known analytical solutions verified correctness. During simulations, we continuously monitored conservation laws as a sanity check. Performance optimizations like sparse matrix storage cut memory usage by 90% for 200×200 grids, vectorized operations eliminated Python bottlenecks, and strategic Numba acceleration boosted critical sections. The modular architecture not only delivered accurate, efficient results but also made the code adaptable for future extensions.

4. Results

4.1. TISE Solutions

The accuracy and computational efficiency of the numerical solutions were strongly influenced by the grid resolution. By using the finite difference method and using 16,000 grid points, we solved for the first four eigenstates of the zero-potential infinite well with a runtime of approximately 2 seconds which is shown in Figure 1. Comparing the numerical eigenenergies with the analytical solutions revealed very small differences, ranging from 0.399% to 0.404%. After normalizing the analytical solution
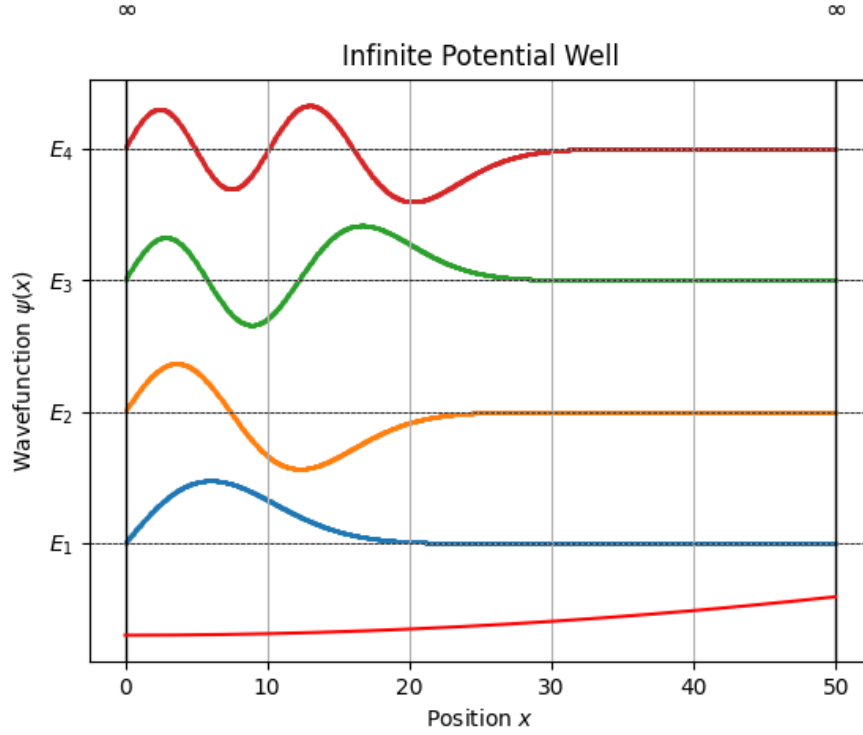
with the grid spacing, we calculated the dot product of the analytical and numerical eigenfunctions, which resulted in a value of 1, indicating perfect overlap. Increasing the number of grid points improved the agreement between the numerical and analytical eigenfunctions, but the eigenenergies showed less sensitivity to the grid size, which is consistent with the expected scaling of accuracy as approximately $\frac{1}{\sqrt{N}}$.
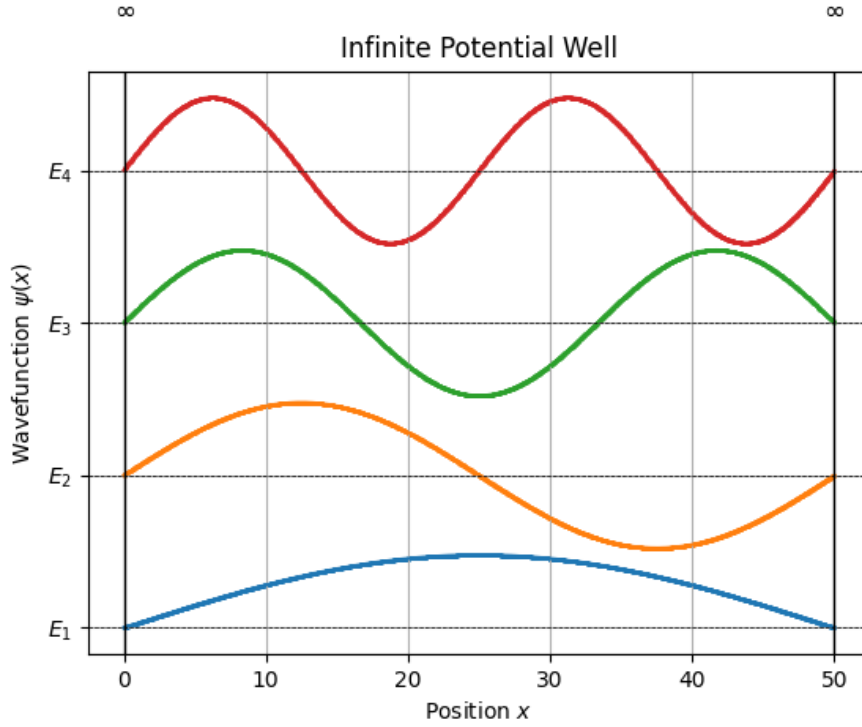
n	Numerical EValue (J)	Analytical EValue (J)	Difference (%)	Dot Product
1	1.97e-03	1.97e-03	3.99e-01	1.00e+00
2	7.86e-03	7.90e-03	4.00e-01	1.00e+00
3	1.77e-02	1.78e-02	4.02e-01	1.00e+00
4	3.15e-02	3.16e-02	4.04e-01	1.00e+00

Figure 1: Plot of the first four eigenstates of a zero-potential infinite well. The accompanying table shows the numerical and analytical energies of the first four states, the difference between them, and the dot product of the analytical and numerical eigenstates.

We introduced a HQSHO perturbation to the zero-potential infinite well with a perturbation coefficient, $\lambda = 10^{-8}$ and $\omega = 1$. Solving for the first four eigenstates resulted in odd numerical eigenfunctions, which is consistent with the analytical expectations. The corresponding eigenfunctions and eigenenergies areshown in Figure 2. The comparison between the analytical and numerical eigenenergies revealed a difference ranging from 0.228% to 0.756%, with larger differencesobserved at higher energy levels. The dot product was not calculated due to the complexity of the analytical eigenfunction solution. The HQSHO perturbation case showed less accurate results compared to the zero-potential cases. This may be due to the small magnitude of the perturbation coefficient, which could reduce the numerical precision needed to resolve the subtle shifts in eigenenergies and eigenfunctions. Additionally, second-order finite difference methods were used throughout, which generally provide good accuracy but may struggle to resolve small perturbative effects unless extremely fine grids are used.

Figure 2: Plot of the first four eigenstates of a zero-potential infinite well with a HQSHO perturbation. The shape of the potential is shown below the first eigenstate. The accompanying table shows the numerical and analytical energies and the difference between them.

By generalizing the TISE to 2D, we used a grid size of 5,000 points to solved for the first four states of the 2D zero-potential infinite well with a runtime of 5 seconds. This resulted in two degenerate states ψ_{12} and ψ_{21}, and two non-degenerate states, ψ_{11} and ψ_{22}, which are shown in Figure 3. The analytical solutions were also calculated, and the difference between the analytical and numerical solutions ranged from 3.50% to 3.58%. The dot products showed better overlap of the eigenfunctions for the degenerate states, with values of 0.99, and for the non-degenerate states, the overlap was 0.75. This slightly lower accuracy could be due to the numerical resolution being insufficient to capture the fine differences between nearly degenerate states or the increased sensitivity of degenerate states to boundary conditions. Memory limitations and processor capacity also imposed constraints on grid size, particularly for the 2D cases, which limited how accurately higher-energy states be resolved.

For the HQSHO perturbation of the zero-potential infinite well in 2D, we solved for the numerical eigenfunctions and eigenenergies, which are shown in Figure 4. However, due to their complexity, we were unable to compute the analytical eigenenergies and eigenfunctions for comparison.
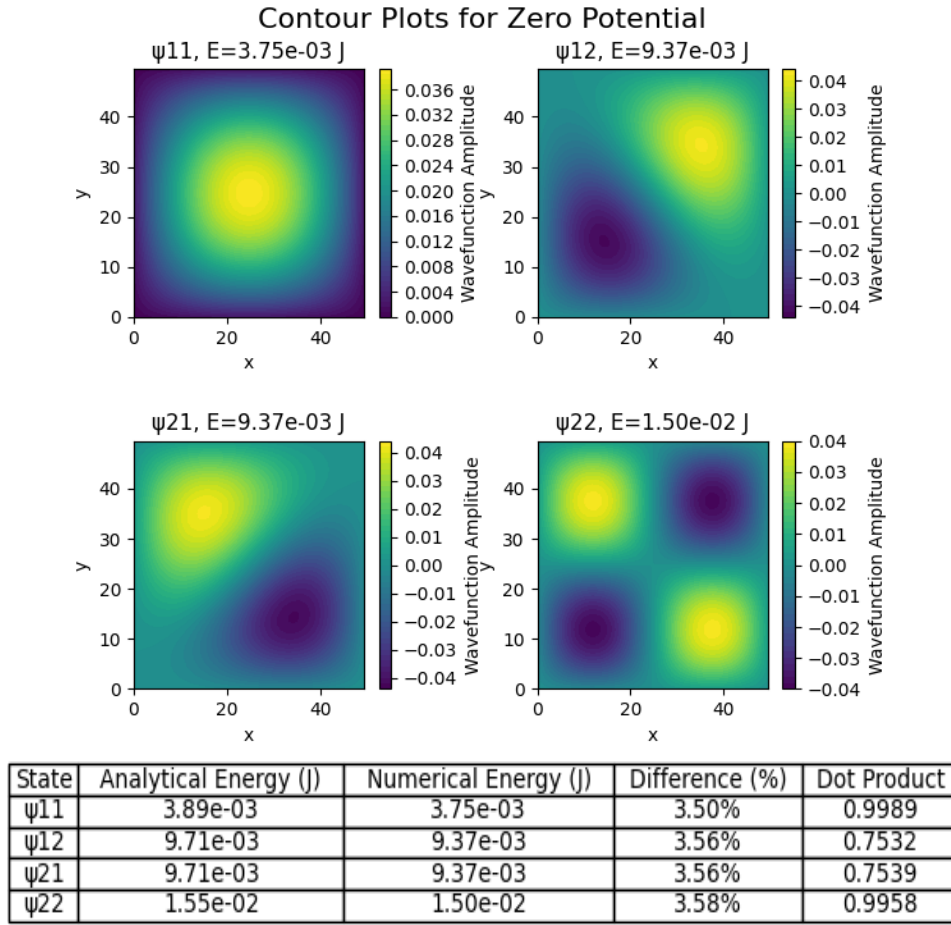
Contour Plots for Zero Potential

State	Analytical Energy (J)	Numerical Energy (J)	Difference (%)	Dot Product
ψ11	3.89e-03	3.75e-03	3.50%	0.9989
ψ12	9.71e-03	9.37e-03	3.56%	0.7532
ψ21	9.71e-03	9.37e-03	3.56%	0.7539
ψ22	1.55e-02	1.50e-02	3.58%	0.9958

Figure 3: Contour plot of the first four eigenstates of a zero-potential infinite well in 2D. The accompanying table shows the numerical and analytical energies of the first four states and the difference between them.
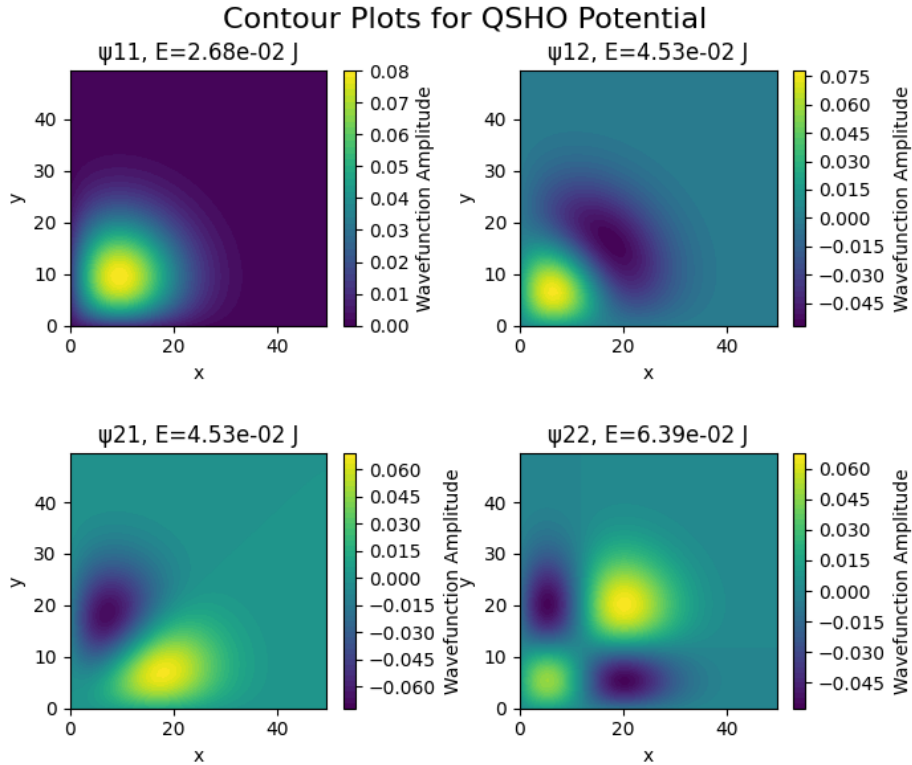
Contour Plots for QSHO Potential

Figure 4: Contour plot of the first four eigenstates of a zero-potential infinite well with a HQSHO perturbation in 2D.

4.2. TDSE Solutions

A Gaussian wave packet was introduced at the centre of a zero-potential infinite well. By applying the expansion method, we decomposed the initial wave packet into the first four eigenfunctions of the potential well. These were then used to solve the TDSE using the finite difference method to simulate the wave packet's evolution over time. The animation also highlights the most probable position of the wave packet at each time step. A frame from the animation is shown in Figure 5.
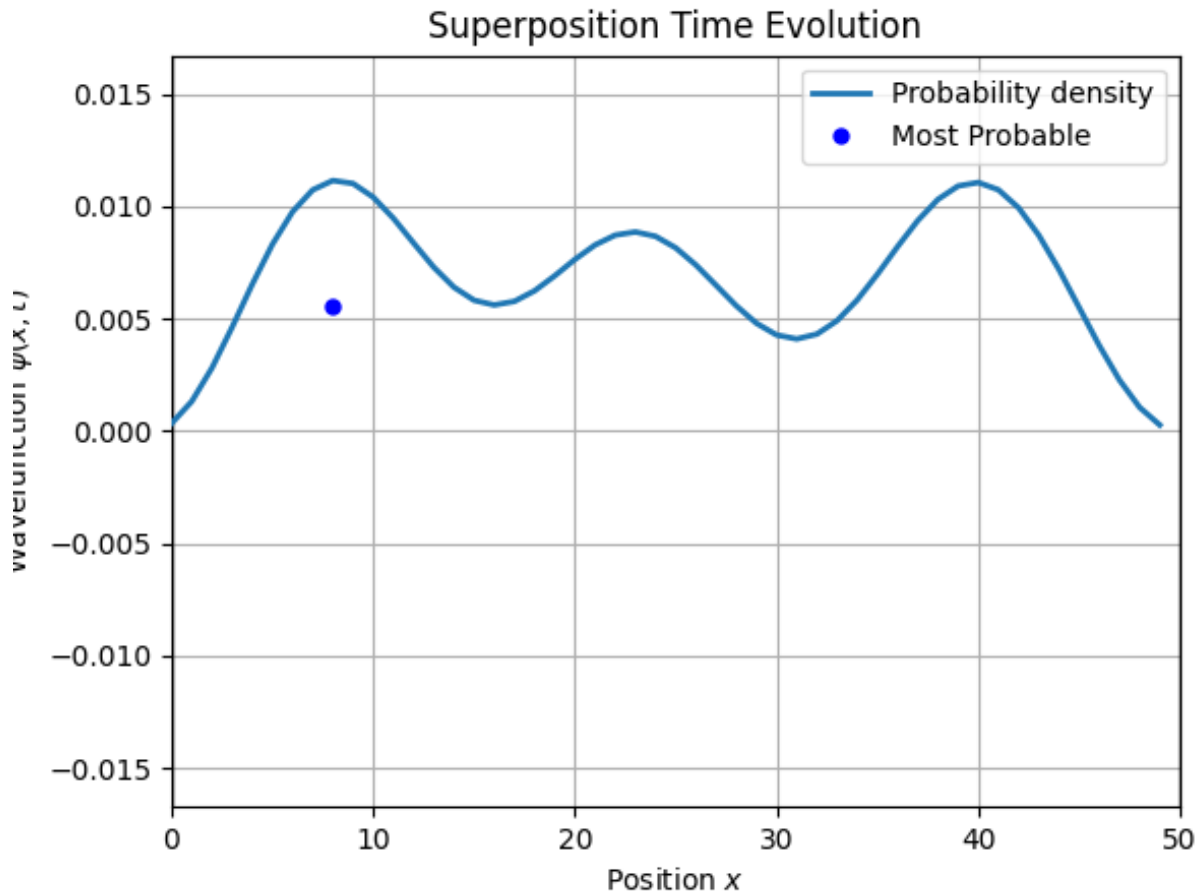

Figure 5: Frame showing the evolution of a Gaussian wave packet inside a zero-potential infinite well, traveling from left to right. The figure depicts the wave packet after it has hit the walls multiple times, showing the most probable of the particle.

By extending the 1D case, we solved the TDSE for a 2D zero-potential infinite well. Using the expansion method, we decomposed the initial wave packet into the first 4 eigenfunctions and observed its behavior, which closely resembled the 1D case. Figures 6 and 7 display three frames from the animations for both the zero-potential and HQSHO-perturbed wells. In both cases, the wave packet starts at the center of the well and propagates in all directions. For the zero-potential well, the wave evolves from the highest energy state, initially displaying 16 peaks, which gradually transition to 9, then 4, then 1, before repeating periodically. In the HQSHO-perturbed well, we observe a similar behavior, but with a key difference: the potential well has a minimum potential at [0,0], causing the wave to travel toward this minimum. As a result, higher amplitudes are observed closer to it.
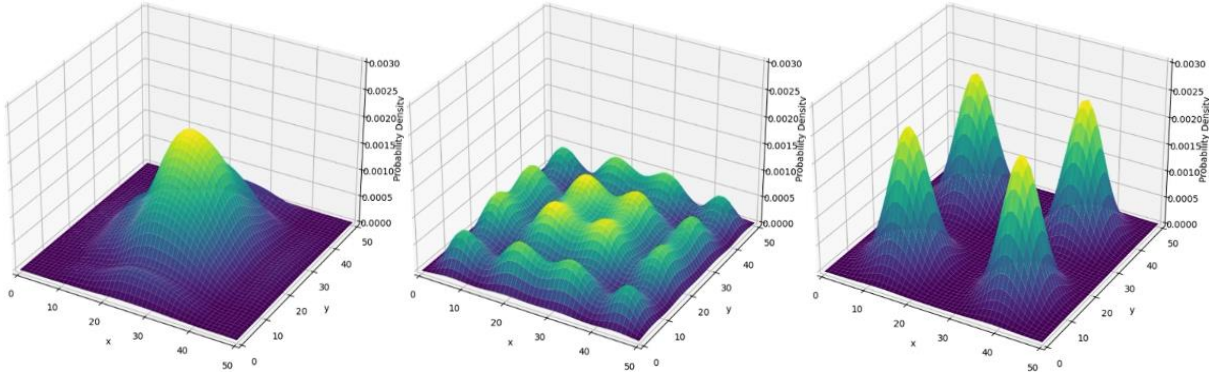
Figure 6: Three frames showing the evolution of a Gaussian wave packet inside a 2D potential well, initially introduced at the centre of the well and traveling in all directions. The frames, presented from left to right, depict the wave packet's evolution over time.
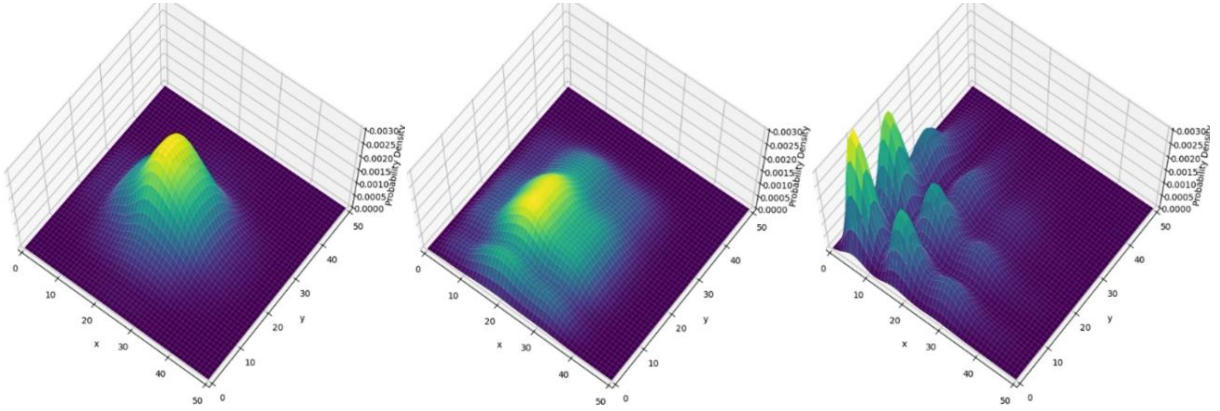

Figure 7: Three frames showing the evolution of a Gaussian wave packet inside a 2D potential well with a half quantum simple harmonic oscillator (HQSHO) perturbation, initially introduced at the centre of the well and traveling in all directions. The frames, presented from left to right, depict the wave packet's evolution over time.

4.3. Potential Barriers and Quantum Tunnelling

To investigate quantum tunnelling, we introduced a Gaussian wave packet with energy $E = 50J$, initially positioned at $x_0 = 5m$, traveling from left to right inside a zero-potential infinite well. A frame from the animation is shown in Figure 8. Within the potential, we added a barrier of width $a = 0.2m$ and height $V = 90J$. By calculating the analytical reflection and transmission coefficients and comparing them to the numerical values which were determined by looking at the change in amplitude of the wave, we observed a difference of 1.26% for the reflection coefficient and 2.19% for the transmission coefficient which is shown in Figure 8. These close agreements were achieved by employing the Crank-Nicolson method, which enabled us to increase the number of grid points to 40,000 while maintaining numerical stability and accuracy. Its implicit nature and time-reversibility contributed to the precision of our numerical results, even for larger grid sizes.

Potential Barriers and Gaussian Wave Packet
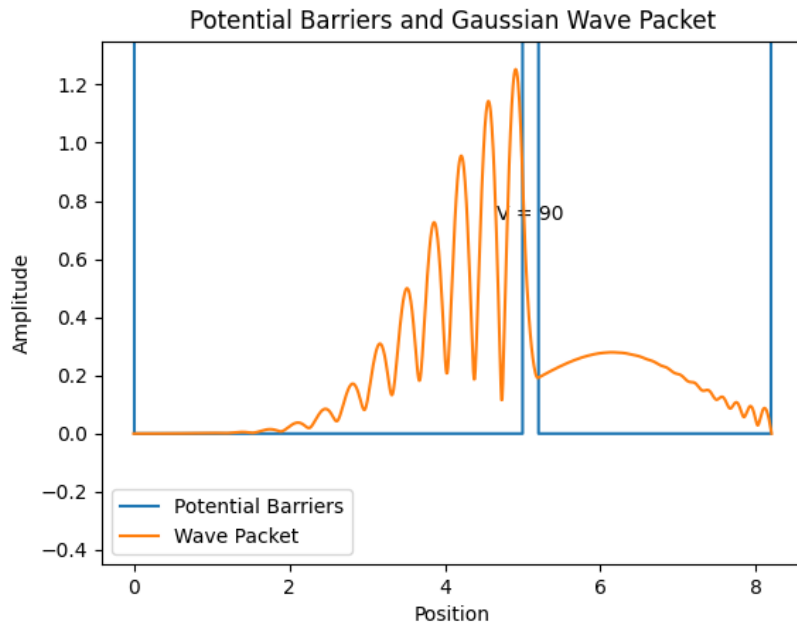
Coefficient	Numerical	Analytical	Difference (%)
Reflection (R)	0.88	0.89	1.26
Transmission (T)	0.11	0.11	2.19

Figure 8: Frame showing a Gaussian wave packet traveling from left to right inside an infinite potential well, encountering a barrier of height V = 90 J. The accompanying table shows the numerical and analytical reflection and transmission coefficients, along with the difference between them.

We generalized the code to examine the behavior of the Gaussian wave packet within a 2D zero-potential infinite well. To simulate the double-slit experiment, we introduced three substantially large barriers at $x = [15,15.5]$m creating double slits of width 0.15 m and spacing of 0.9m between them. A Gaussian wave packet was introduced at $x_0 = 5$, traveling in the positive x-direction to observe how the wave evolves as it encounters the barriers. Three frames of the animation are shown in Figure 9. A data logger was placed at the $x = 40$ plane, capturing the wave intensity and showing the accumulated intensity at each point on the y-axis. The resulting pattern confirmed the expected interference fringes [5], though some noise was observed due to reflections from the sides of the well and their interactions with the logger plane.
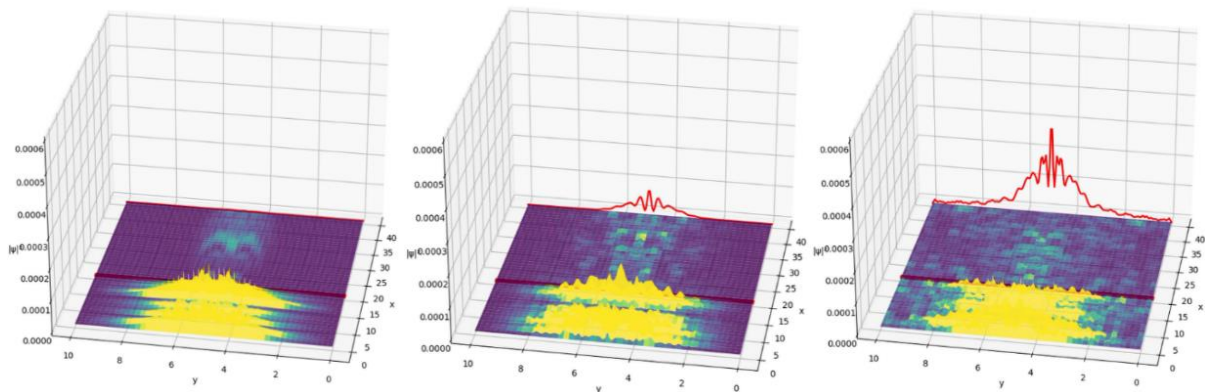

Figure 9: Three frames demonstrating the double slit experiment using potential barriers inside a 2D zero potential infinite well. The intensity logger captures the accumulated intensity over time. The frames are presented from left to right.

11

5. Conclusion

This project successfully solved the Time-Independent and Time-Dependent Schrödinger Equations in 1D and 2D using numerical methods, providing insight into quantum behaviour across various potential configurations. The finite difference method produced accurate eigenfunctions and eigenenergies for the infinite well, with results closely matching analytical solutions. Wave packet evolution was analysed using both explicit and implicit methods, with the Crank-Nicolson method improving stability and accuracy, particularly in quantum tunnelling simulations. However, computational constraints limited grid resolution, affecting the precision of degenerate states and perturbation results, while interference patterns in the 2D barrier simulation displayed some noise due to boundary reflections.

Future work could focus on deriving analytical solutions for the 2D perturbed system to enable direct comparison with numerical results. Extending the method to 3D would allow for modelling hydrogen-like orbitals, providing further validation of numerical techniques. A more detailed study of interference patterns could confirm whether the observed wave behaviour follows expected diffraction patterns, as predicted in classical wave optics. Investigating more complex potentials, such as those representing positive holes in semiconductors, could lead to quantum simulations of electron behaviour in p-n junctions. Additionally, improving computational efficiency with adaptive grids or higher-order numerical methods would enhance accuracy while reducing runtime, making these simulations more feasible for larger systems.

References

[1] Schrödinger, E., "Quantization as a Problem of Proper Values, Part I," *Annalen der Physik*, Vol. 79, 1926, pp. 361–376.

[2] Crank, J., and Nicolson, P., "A Practical Method for Numerical Evaluation of Solutions of Partial Differential Equations of the Heat-Conduction Type," *Proceedings of the Cambridge Philosophical Society*, Vol. 43, No. 1, 1947, pp. 50–67.

[3] Richardson, L. F., "The Approximate Arithmetical Solution by Finite Differences of Physical Problems Involving Differential Equations, with an Application to the Stresses in a Masonry Dam," *Philosophical Transactions of the Royal Society A*, Vol. 210, 1911, pp. 307–357.

[4] Schrödinger, E., "Über die Störungstheorie," *Annalen der Physik*, Vol. 80, No. 4, 1926, pp. 437–490.

[5] Young, T., "Experiments and Calculations Relative to Physical Optics," *Philosophical Transactions of the Royal Society of London*, Vol. 94, 1804, pp. 1–16.

The number of words in this document is 2995.